2015

Global survey of concentric gravity waves in AIRS images and ECMWF analysis

Jie Gong
Universities Space Research Association, Columbia, Maryland, Jie.Gong@nasa.gov

Jia Yue
Hampton University

Dong L. Wu
Climate and Radiation Laboratory, NASA Goddard Space Flight Center, Greenbelt, Maryland

AGU PUBLICATIONS

JGR

Journal of Geophysical Research: Atmospheres

RESEARCH ARTICLE
10.1002/2014JD022527

Key Points:
- First climatology of concentric gravity wave (CGW) in the stratosphere
- Concentric ring wave characteristics have strong diurnal variations
- ECMWF-resolved CGWs mimic the AIRS observation well with some discrepancy

Correspondence to:
J. Gong,
Jie.Gong@nasa.gov

Citation:
Gong, J., J. Yue, and D. L. Wu (2015), Global survey of concentric gravity waves in AIRS images and ECMWF analysis, *J. Geophys. Res. Atmos.*, *120*, 2210–2228, doi:10.1002/2014JD022527.

Received 2 SEP 2014
Accepted 13 FEB 2015
Accepted article online 19 FEB 2015
Published online 21 MAR 2015

Global survey of concentric gravity waves in AIRS images and ECMWF analysis

Jie Gong[1,2], Jia Yue[3], and Dong L. Wu[2]

[1]Universities Space Research Association, Columbia, Maryland, USA, [2]Climate and Radiation Laboratory, NASA Goddard Space Flight Center, Greenbelt, Maryland, USA, [3]Department of Atmospheric and Planetary Sciences, Hampton University, Hampton, Virginia, USA

Abstract Concentric gravity waves (CGWs) are atmospheric phenomena with ring-shape perturbations originating in the troposphere. They can propagate up to the ionosphere and thermosphere and dynamically couple the lower and upper atmosphere. In this study we developed a novel ring detection algorithm to extract CGWs from the Atmosphere Infrared Sounder (AIRS) radiance data and the European Center for Medium-Range Weather Forecasting (ECMWF) analysis temperature in the stratosphere to produce the first global maps of such phenomena. The algorithm is capable of estimating wave amplitude, wavelength, propagation direction, and source location. Both AIRS and ECMWF data show a significant diurnal variation in wave propagation direction and generation, in addition to strong seasonal variations in wavelength and amplitude. Occurrence of these ring waves is associated not only with tropical deep convections but also with summertime midlatitude convection, wintertime extratropical jets, and topography such as islands. The high-resolution ECMWF analysis data capture most of the CGW features, but the wave amplitude is significantly weaker than AIRS observations, showing few convectively generated CGWs.

1. Introduction

Gravity waves (GWs) are ubiquitous in the atmosphere as the product of restoring gravity force and air buoyancy. GWs play a key role in coupling middle and upper atmosphere dynamics by transporting and depositing wave energy and momentum fluxes in the mean flow. The most prominent GW sources are convection (e.g., isolated thunderstorms, tropical cyclones, and squall lines), elevated topography (e.g., South Pacific islands and Andes), and frontal systems/imbalanced flows [*Jiang and Wu*, 2001; *Jiang et al*., 2003, 2004a, 2004b; *Fritts and Alexander*, 2003; *Plougonven and Zhang*, 2014]. After being excited in the troposphere, GWs carry some unique characteristics of their sources, which are often reflected in wavelength, period, amplitude, and shape of wave fronts. For instance, linear GWs (i.e., wave streets) can be excited by a line source such as cold fronts and extended mountain ridges [e.g., *Smith et al*., 2009], whereas wake-like patterns are indicative of a point source (e.g., islands) beneath an atmospheric flow. In the absence of the background wind, circular or nearly concentric GWs (CGWs) may be produced from point sources, as reported in the case studies of isolated thunderstorms and small islands [e.g., *Yue et al*., 2009; *Grimsdell et al*., 2010; *Alexander and Grimsdell*, 2013]. GW morphology has a unique importance in helping identify remote wave sources and facilitating teleconnection studies between the lower and upper atmosphere [*Yue et al*., 2013, 2014b].

CGWs can in turn modulate and interact with convection and precipitation as revealed in the study of typhoon development [*Mapes*, 1993; *Kim and Chun*, 2011]. Breakdown of CGWs also produces turbulence and mixing near the tropopause, causing aviation hazards [*Lilly*, 1978; *Hines*, 1988]. The CGWs with a fast phase velocity can propagate through the atmosphere without encountering much critical-layer filtering by the background flow. Sometimes, they are partially filtered under an atmospheric flow where half of the ring pattern is subjected to the critical-layer breaking. For those unfiltered, they are able to enter the upper atmosphere and perturb the thermosphere and ionosphere [*Hines*, 1960; *Vadas and Liu*, 2009], causing the spread F from seeding mesoscale equatorial ionospheric disturbances [e.g., *Fritts et al*., 2008; *Krall et al*., 2013], electron density, and ratio wave scintillations.

CGW events have been observed from space in the 4.3 and 15 μm CO_2 band radiances [e.g., *Dewan et al*., 1998; *Eckerman et al*., 2007; *Hoffmann and Alexander*, 2010; *Grimsdell et al*., 2010; *Gong et al*., 2012], polar mesospheric clouds [*Yue et al*., 2014a] and nightglow images [*Miller et al*., 2012; *Yue et al*., 2014b]. They can

also be seen in ground-based mesopause nightglow images [e.g., *Taylor and Haphood*, 1988; *Sentman et al*., 2003; *Suzuki et al*., 2007; *Yue et al*., 2009, 2013]. In the event of strong earthquakes/tsunamis or deep convection, concentric ring patterns are evident in the ionospheric Total Electron Content (TEC), which is induced by the CGWs propagating into the ionosphere [*Tsugawa et al*., 2011; *Nishioka et al*., 2013].

Despite numerous reports of CGW events, there is by far no global climatology of these waves. This is mainly due to the fact that it is difficult to isolate the ring pattern from other perturbations as CGWs often emerge in a transient and unpredictable manner. In addition, CGWs often have a partial ring pattern, which requires a sophisticated algorithm to extract the wave properties. Without observational guidance on wave property and global distribution, it is difficult to develop a realistic representation of CGWs and their effects in general circulation models (GCMs) [*Richter et al*., 2010; *Geller et al.,* 2013]. Thanks to the rapid advance of GCM spatial and temporal resolution, a large portion of GWs can now be resolved explicitly in GCMs [*Yamashita et al*., 2010; *Sato et al*., 2012; *Preusse et al*., 2014], including the CGWs as discussed above. If the wave sources are adequately represented in these models, CGWs should appear and propagate in the upper atmosphere. Thus, the observed CGWs provide a valuable diagnosis of high-resolution global models and analysis data such as those from European Center for Medium-Range Weather Forecasting (ECMWF).

To investigate global CGW distribution and wave properties, we developed a novel, robust algorithm to extract ring-shape patterns from satellite and model data. We have applied the method successfully to the Atmospheric Infrared Sounder (AIRS) radiance data and the ECMWF analysis data for CGW detection. We obtained, for the first time, the global distribution of CGWs in the middle atmosphere and their seasonal variations.

The paper is organized as follows: The ring detection algorithm will be presented in section 2, followed by the global distribution of CGW characteristics derived from AIRS radiance data in section 3. The same distribution from ECMWF analysis temperature data will be presented and compared with AIRS observation in section 4, and section 5 concludes the paper.

2. Data Sources and Methodology

2.1. AIRS Data

Launched in 2002, AIRS is a hyperspectral infrared spectrometer and sounder onboard the polar-orbiting Aqua satellite. It has 2378 spectral channels to cover the 3.74–4.61 μm, 6.20–8.22 μm and 8.8–15.4 μm bands. The AIRS cross-track scan produces 90 footprints over a 1650 km swath every 2.67 s [Aumann and Miller, 1994], and the outermost scan angles are ±48.95° from nadir. The footprint size increases from $13.5 \times 18\ km^2$ at nadir to $32.5 \times 18\ km^2$ at the swath edge. Because of its wide swath, AIRS can resolve waves with a horizontal wavelength between 50 and 1650 km in principle.

AIRS has the advantage of being able to observe CGWs that are associated with high frequency, long ($>$12 km) vertical wavelength on the mesoscale ($<$1650 km) [*Gong et al*., 2012]. The AIRS broad weighting function (WF) makes it insensitive to inertia GWs (i.e., with short vertical wavelengths). As revealed in high-resolution model simulations, CGW structures are usually tilted away from their tropospheric sources while the waves propagate upward. According to the GW dispersion relation, the higher the CGW frequency, the more vertically it is tilted. Previous GW studies on AIRS 15 μm and 4.3 μm radiances showed strong correlation between the observed GW amplitude and deep convective activity in the summer hemisphere and in the tropics [*Hoffmann and Alexander*, 2010; *Gong et al*., 2012]. These AIRS channels have a weighting function peaking at various altitudes in the stratosphere. Deep convection is a type of perturbation with a rich power spectrum at long vertical wavelengths. The AIRS-observed tropical GWs were later used to constrain convective Gravity Wave Drag (GWD) parameterizations in GCMs [*Choi et al*., 2012]. In addition, mountain waves are another source of perturbations with long vertical wavelengths. *Gong et al*. [2012] and *Hoffmann et al*. [2013] found strong GW activities above elevated topography and islands at the middle-to-high latitudes.

To develop and demonstrate the ring-pattern detection method, here we focus on the AIRS radiance data at 2.5 hPa (~40 km). The full width half maximum (FWHM) of this channel is ~12 km, useful for studying waves with vertical wavelengths greater than 12 km. Similar to the procedure used in *Gong et al*. [2012], we first remove the cross-track background with a third-order polynomial fit for each half of the swath. This analysis procedure effectively removes the background limb-brightening effect as well as planetary waves at scales $>$ 800 km and/or other large-scale temperature gradients. The next step is to remove the

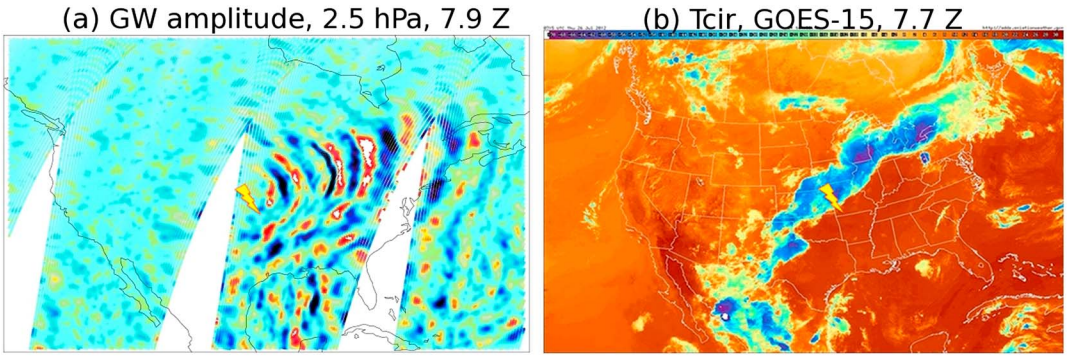

Figure 1. (a) A concentric ring event (radiance perturbation) occurred over the Continental United States at about 7.9 UTC on 26 July 2012 and was observed by AIRS CH#75 during its descending overpasses. The figure is smoothed by 3×3 running window for display purposes. Color scale is linear and ranges from −0.4 K (blue) to +0.4 K (red). (b) Corresponding tropospheric cloud systems (cloud-induced radiance perturbation "Tcir") observed by GOES-15 at 7.7 UTC (http://adds.aviationweather.gov). Color scale is linear and ranges from −70 K (purple) to +30 K (red). The estimated ring center is marked by a yellow lightning bolt in both panels. See text for details.

along-track background with a 13-point running mean (~250 km). The resulting residuals are considered as "perturbations" that include measurement noise, random atmospheric oscillations, and GWs. The running smooth window effectively removes the mean background field and slowly varying planetary wave features. The corresponding detection threshold for the GW variance is $(1/M)\sigma_e^2$, where M is the window size (unit is number of FOV), and we use noise equivalent delta temperature (NEdT) of CH#75 to represent σ_e [*Wu and Eckermann*, 2008; *Gong et al*., 2012]. Therefore, the minimum brightness temperature perturbation (σ_{GW}) for a GW event is 0.08 K at CH#75. Note that the noise level should be slightly higher at winter hemisphere high latitude [*Hoffmann et al*., 2014]. While further averaging certainly reduces the channel noise, information from the boundary $M/2$ number of observations is lost due to running smooth averaging. This is undesirable for detecting GWs with longer horizontal wavelength (across-track) or GWs that occur near the polar region (along-track). While *Gong et al*. [2012] applied a sevent-point running window to further extract GW signals across-track, this method arbitrarily imposes a sensitivity window to extract mesoscale GWs, which may not include all concentric ring cases that are detectable by AIRS (see their Figure 2 for details). In this paper, no more filters are further applied, and all AIRS detectible GW signals should be kept. The 4.3 μm CO_2 channels can also serve as a good choice for detecting CGWs as suggested by *Hoffmann and Alexander* [2009, 2010]. The advantages and disadvantages of 15 and 4.3 μm channels are discussed in Appendix A.

Stratospheric CGWs are often associated with strong convective activities in the troposphere. As shown in Figure 1, the ring patterns in the 2.5 hPa AIRS radiance are collocated with a cold front passing through Nebraska and Iowa in the Geostationary Earth Satellite (GOES) image. From midnight of July 25 to the early morning of 26 July 2012, the cold front "became active and thunderstorms developed" with hail and damaging gusty wind in those states (www.crh.noaa.gov/arx/?n=jul2512; www.spc.noaa.gov/exper/archive). Later on, several tornados formed and touched down on the evening of 26 July. Deep propagating ring waves were excited spontaneously around the same time the thunderstorms developed (Figure 1a). Due to the critical-level filtering in the stratosphere, only half of the CGW structures (i.e., the eastward propagating waves) survived, while the other half (the westward propagating waves) was selectively removed by the westward background wind in the stratosphere. This is typically seen during a summer day over North America, where the Great Plains are a hotspot for nightglow concentric GWs. The visually estimated ring center (yellow lightning bolts in Figure 1) collocated with a developing deep convection center (as identified by the region of Tcir < -50 °C) around the same time (Figure 1b). The Tcir (cloud-induced radiance perturbation) in Figure 1b, defined as the difference between the observed radiance and the modeled clear-sky background [http://adds.aviationweather.gov; *Gong and Wu*, 2014], provides a proxy of ice cloud optical thickness. Blue/purple colors in Figure 1b hence represent cold high ice clouds or vigorously developing convective centers. In this case, deep convection is clearly a primary source of stratospheric CGWs. However, this does not preclude small concentric rings with horizontal wavelengths on the order of 10 km, which are commonly seen in ground-based airglow imagers. Those small scale CGWs are hardly

discernable by AIRS due to coarse resolution of space borne sensors [*Yue et al*., 2013]. The resolution effect, along with curved wave fronts, will be discussed in further detail in section 3.

2.2. ECMWF Analysis

GW-induced drag (GWD) must be parameterized in the models with coarse resolution such as GCMs. The balance between resolved and parameterized GWs continues to evolve as the model resolution improves. On the one hand, the GWD scheme needs to be retuned when GCMs adapt a new resolution, or when the scheme is applied to a different GCM. On the other hand, most of the current GWD schemes are highly simplified (e.g., uniform distribution and no latitudinal dependence), and some GW sources are even completely missing (e.g., jet imbalance). In other words, the GWD development is not synchronized or interactive with the changing technology. With the fast advance of computational power in supercomputers, GCMs are now running on increasingly higher resolutions, leading to more resolved GWs and more realistic wave-mean flow interactions. Instead of criticizing GWD parameterization schemes, nowadays there are perhaps more questions on the resolved GWs. Are those resolved GWs in high-resolution GCMs realistic? What model resolution is needed in order to resolve the entire GW spectrum? For these motivations, AIRS observations serve as an ideal touchstone of GCM representation of GW sources.

The numerical prediction model at ECMWF, one of the most sophisticated high-resolution GCMs in the world, has been used to answer these types of questions by comparing model-resolved GWs with observations. *Schroeder et al*. [2009] compared the resolved GWs in ECMWF with Sounding of the Atmosphere Using Broadband Emission Radiometry (SABER) observations and found that GWs from topographic sources were as twice strong in SABER as those in ECMWF analysis while GWs from tropical deep convections were poorly correlated. *Preusse et al*. [2014] studied wave properties (e.g., wavelength and momentum flux) in ECMWF against the High Resolution Dynamics Limb Sounder (HIRDLS) measurements and concluded that ECMWF-resolved convective GWs are weaker in amplitude and longer in horizontal wavelength. Both studies used observations from limb (sublimb) sounders, which only addressed a subset of the GW spectrum (i.e., short vertical and long horizontal wavelengths), while the other part of the wave spectrum (long vertical and short horizontal wavelengths), including CGWs, has not been evaluated [*Wu et al*., 2006]. While convection is a major CGW source, such a comparison conducted in the current study would be especially meaningful to guide the future direction of improving GCM representation of deep convections.

In this study, we analyzed the 6-hourly ECMWF analysis data for January and July 2010 to evaluate the resolved CGW properties. Starting on 26 January 2010, ECMWF forecast model had been upgraded from T799 to T1279, corresponding to a grid size of 25 km to 16 km, respectively. Although, in principle, the resolvable wavelength is 6 times larger than the model grid size, the actual resolution is poorer than that due to additional damping in GCM to prevent instability from growing. *Preusse et al*. [2014] suggested that the smallest detectable wavelength without significant damping should be around 8 times the grid size, corresponding to ~130 km for T1279 and ~200 km for T799. Both scales fall into the horizontal wavelength observational range of AIRS GWs. We use the January 2006 data to evaluate effects of the increased model resolution on resolved GWs (27–31 January data are excluded). In both analysis data sets, the inner loop is still T255, implying that the observed GW spectra were mostly not assimilated except those inertial GWs with extremely low frequency and long horizontal wavelength. Therefore, the resolved GWs in the analysis data are mostly generated by the model.

In order to compare GWs sampled and measured under similar conditions, we create "synthetic AIRS GWs" from the ECMWF data by applying the AIRS observational filter to the data. We first convolved AIRS's WF at 2.5 hPa with ECMWF temperature profiles to produce radiance as if it were measured by AIRS in terms of brightness temperature (TB) and then sampled these TBs using the AIRS orbit and viewing geometry to yield the synthetic AIRS radiances. The 6-hourly ECMWF data are interpolated to the AIRS sampling local times to produce data that closely coincides as much as possible. Considering that AIRS passes the equator at local time 1:30 A.M. and 1:30 P.M., both of which are not at the peak or trough of the diurnal cycle of tropical deep convections, we expect the linear interpolation over time should not decrease the capability of capturing the strength of deep convections in ECMWF data. However, the location may not be correct. From the synthetic data, we apply the same ring detection technique for CGW signals.

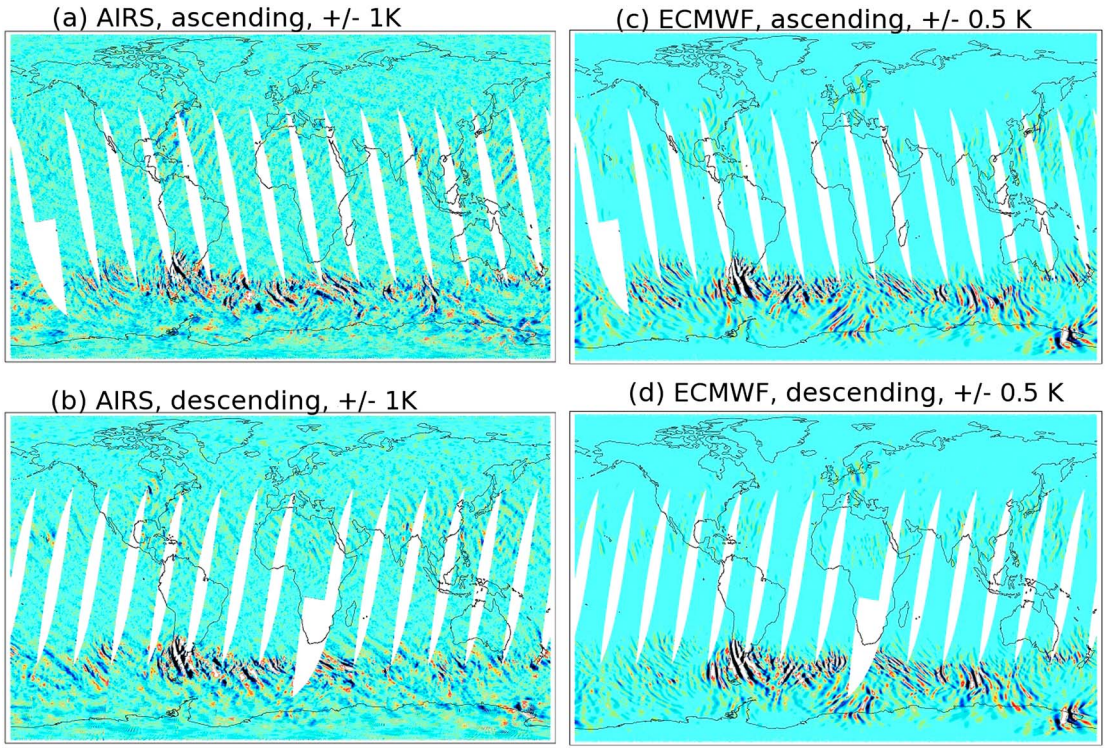

Figure 2. GW amplitudes at ~2.5 hPa from (left) AIRS and (right) ECMWF during AIRS (top) ascending and (bottom) descending orbits on 11 July 2010. A three-point running smooth is further applied to AIRS data, and the color scale is ±1 K. The three-point running smooth is not applied to ECMWF data, and the color scale is ±0.5 K. Details of projecting ECMWF gridded data onto the AIRS observational window can be found in the main text.

Figure 2 shows an example of the resolved GWs from AIRS and the synthetic data at 2.5 hPa on 11 July 2010. High-latitude topographic GWs in the Southern Hemisphere (SH) exhibit the striking wave patterns that are similar to the observations and analysis data in terms of wave directions and wavelengths. The GWs exhibit a possible association with small islands in the Southern Ocean, which were previously reported to account for at least one tenth of the GWD at that latitude band according to the study by *Alexander and Grimsdell* [2013]. The midlatitude belt of GW enhancement in the Southern Ocean is also possibly related to the polar night jet imbalance source [*Jiang and Wu*, 2001], which will be further discussed in sections 3 and 4. Note that the color scales in Figure 2 are different with AIRS being ~2× greater than ECMWF, meaning that the ECMWF-resolved topographic GWs are generally weaker compared to AIRS. In the Northern Hemisphere (NH), ECMWF-resolved convective GWs are weakened even more. In addition, the AIRS observations suggest more meridionally propagating CGWs from convective sources, while ECMWF CGWs are generally too zonal. For the rest of the study, instead of one-on-one comparisons, we chose to evaluate overall performance or monthly statistics of the ECMWF model in CGW generation.

2.3. Ring Detection Algorithm

GWs with horizontal scales of 50–1650 km are retained after background removal for the AIRS data and after convolving with observational filters for the ECMWF data (Figure 2). The following procedures describe detailed steps to extract the CGWs patterns.

First, we need to identify each individual GW event automatically from one observation swath (or orbit). The 2-D wavelet analysis is applied to the entire orbit and selects all statistically significant scenes. If two adjacent scenes are separated by 2° in latitude or more, they are considered as independent GW events. Otherwise, the two scenes represent a single event. To count for a potential overlapping between adjacent swaths, we add a 500 km wide buffer zone on both sides of the identified GW scene and reperform the wavelet analysis on the wider domain. This extra processing allows us to determine if two identified independent GW scenes are overlapping with each other or if they are the "broken" scenes from one wave event. Since we are not to emphasize wave occurrence frequency in this study, the choice of buffer zone size will not impact the results

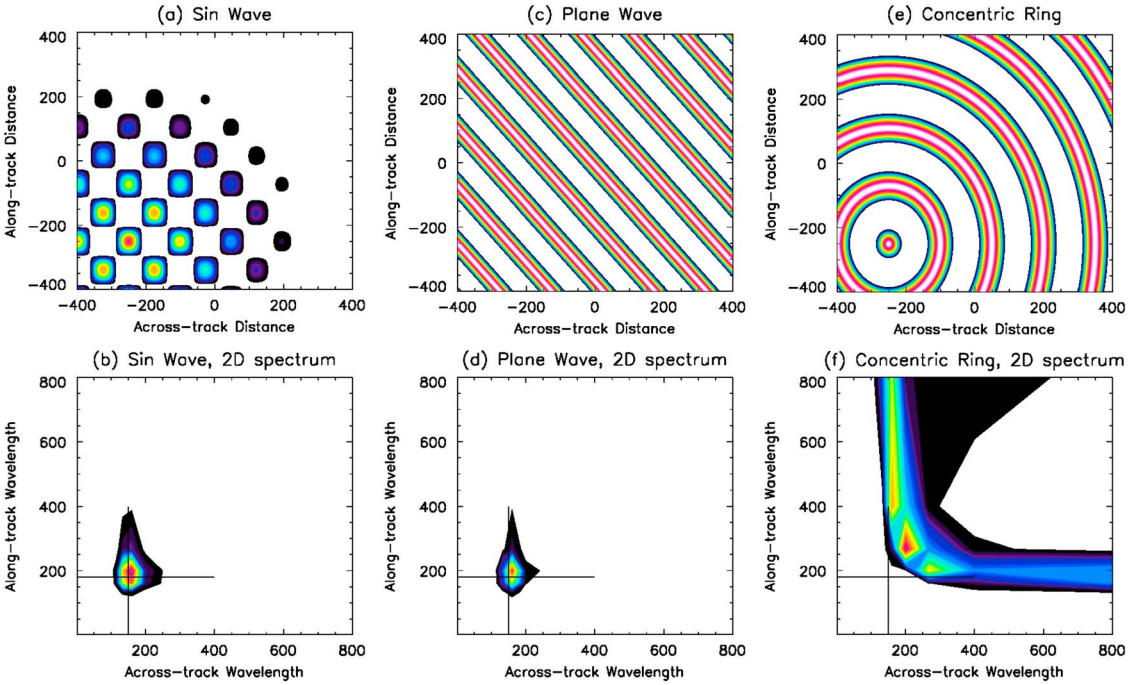

Figure 3. (top) Typical idealized wave patterns (color represents amplitude) and (bottom) their 2-D fast Fourier transform (FFT) spectra (color represents power). The three wave types are (a) sinusoidal, (b) plane, and (c) concentric ring. The color scale is linear with the largest value indicated by red and 0 indicated by white.

presented below. The scene with a significant wave event is further interpolated to a fixed grid (18 km) in the cross-track and along-track dimensions.

The second step is to identify cases where wave fronts resemble the curvature feature, which contains the CGW characteristic. The curved GWs are identified based on the unique "L-shape" of two-dimensional (2-D) Fourier wave power spectrum from the image, which can be clearly seen in Figures 3e and 3f. The 2-D Fourier spectra can reveal different types of GWs: sinusoidal, plane, and ring (Figures 3a, 3c, and 3e). The sinusoidal wave is shown here only for demonstration purpose and rarely occurs in the real atmosphere. In the 2-D spectra panels, we can easily find out that the spectra of the first two have a single peak centered at the dominant across-track/along-track wavelengths because the wavelengths are fixed regardless of the starting point of the image in the analysis. For the ring wave case, the wavelengths vary in both directions, and the 2-D Fast Fourier transformation (FFT) results in a unique "L-shape" spectrum. The largest power aligns with the corresponding across-track/along-track wavelengths (thin black lines in the lower row of Figure 3). These simulated cases assume that the domain of interest is dominated by a single wave, which is also the assumption used for the real data. In the case where wave interferences exists, the estimated wavelength can be affected when two or more waves have comparable amplitudes. The discussion of the interference situation can be found in Appendix B. For the "L-shape" identification, we first find the wavelengths of spectral power greater than the mean by 3× standard deviation and then correlate the data with a series of L-shape delta functions based on the selected cross-track and along-track wavelength combinations (i.e., setting the power amplitude to 1 for all cross-track/along-track solutions at the given along-track/cross-track wavelength combination and to 0 everywhere else). If the correlation coefficient exceeds 0.5, an image with CGW features is found and retained for further analyses.

In the third step to detect a ring wave event, idealized concentric rings from the above wavelength combinations that qualified in the L-shape spectrum are reconstructed, and the rings are patrolled around the entire image to search for the largest correspondence, including the buffer zones. If the largest correlation coefficient is statistically significant, a ring wave event is identified and the ring center is registered. Based on ring size, the significance test is also self-adaptive to the ring radius. Figures 4a and 4b showcase a typical ring wave event, the "L-shape" spectrum, and the ring center is located to the middle left of the entire domain (black contours in Figure 4a). Several rings can be identified from one image.

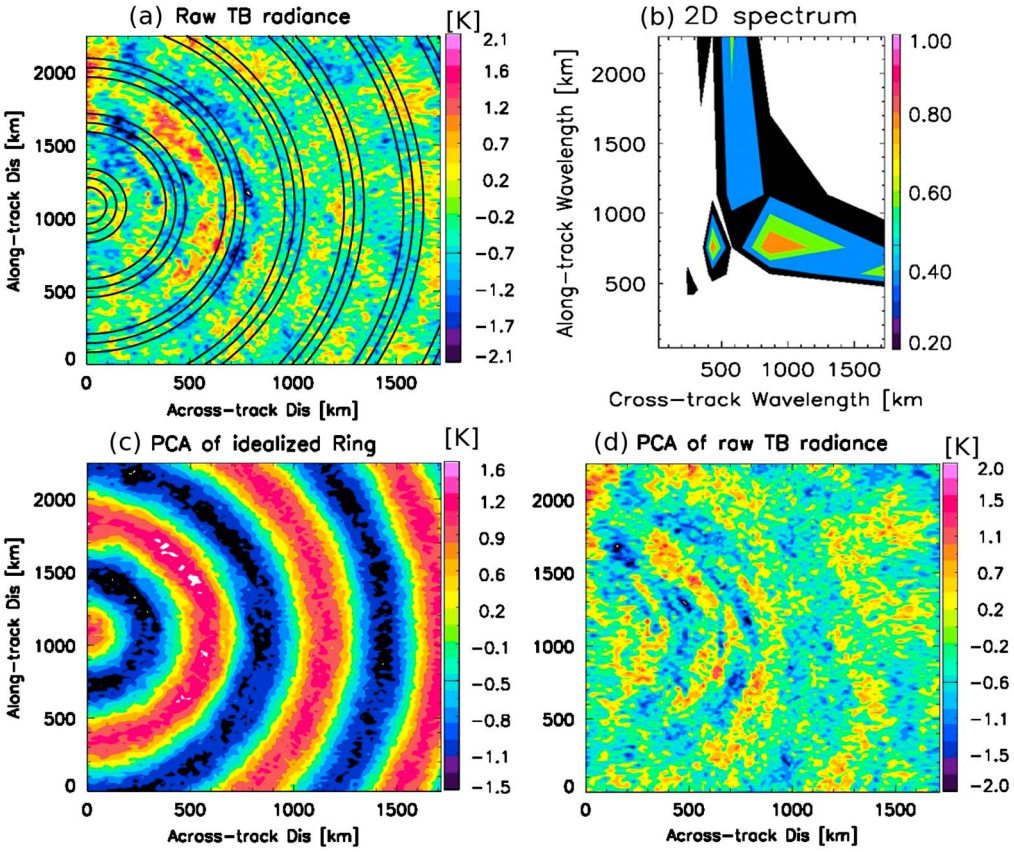

Figure 4. (a) A concentric ring wave event from raw data, (b) the corresponding 2-D spectrum, (c) the PCA projection from the idealized ring fitting to the original image, and (d) the PCA projection from the raw radiance to the idealized image. Color represents wave amplitude in Figures 4a, 4c, and 4d, and the power relative to the maximum power in the entire domain in Figure 4b. Idealized concentric rings are overlaid as black contours in Figure 4a. This event occurred on 14 January 2004 at [40°S, 20°S] and [25°E, 49°E] when Aqua flew along its descending orbit.

Since there is no buffer zone along the cross-track direction, the wave event with ring center located beyond the image's longitudinal range will be missed using the aforementioned method. Similarly, a large wave event occupying two or more orbits would be treated as separate events, which may skew the statistics of wave properties.

After the ring event is identified, the along-track and cross-track wavelength parameters are calculated, and the entire CGW structure can be reconstructed. Figure 4c shows an example of the identified CGW structure projected onto the original image using the Principle Component Analysis (PCA). One can see from Figure 4c that after the PCA is applied, wave phase direction stands out clearly where wave amplitude (i.e., perturbation) is the largest. Therefore, the group of the largest perturbations is used to calculate the mean phase propagation direction from the ring center. The definition of "the largest group of perturbations" could always be variable. In this study, the mean plus triple the standard deviation of the projected image (e.g., Figure 4c) is again used as the standard for "outliers" to represent the most significant signal in wave propagation direction. Randomly chosen cases (~20 cases) were examined using a different criterion (10 grids that have the largest perturbations), and it turned out that the results were qualitatively insensitive to the selection criteria, as the underlying physical meaning is the same.

When the curvature feature of the wave front is not apparent, the propagation direction can be ambiguous to determine. For example, Figure 5b presents a case in the Southern Ocean, where the prevailing zonal wind at 2.5 hPa is westerly. Although visual inspection suggests that the ring center is southeast of the strongest wave fronts, the fitted ring with center located to the northwest yielded the largest correlation coefficient with the original image. Since AIRS prefers to see relatively large-scale and lower frequency GWs

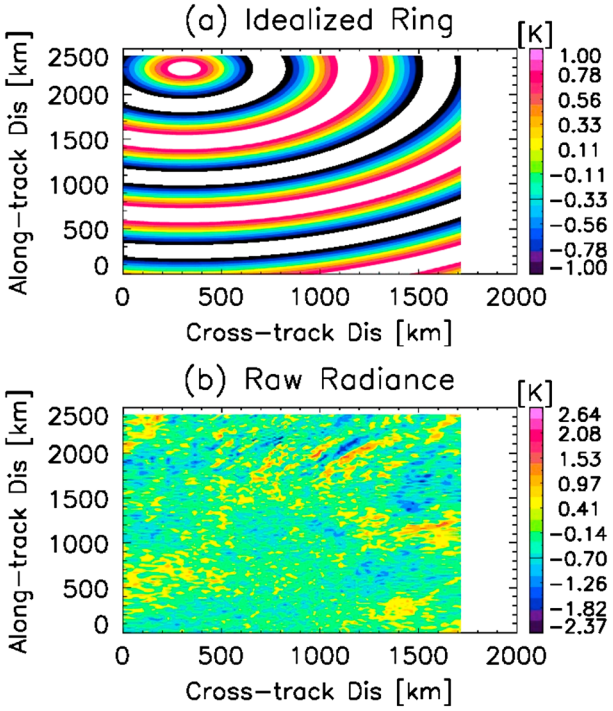

Figure 5. Spurious estimation of ring center and wave propagation direction that satisfies all ring-fitting requirements, where the actual ring phase propagates westward. (a) The best-fit idealized ring. (b) The ring structure from the raw radiance image. This event occurred on 10 July 2007 at [69°S, 44.5°S] and [46.7°W, 4.7°W] when Aqua flew along its ascending orbit. An additional wind-filtering assumption is therefore needed to remove the ill-fit cases like this.

compared to instruments such as airglow imagers, the horizontal phase velocity also tends to be slower, meaning that they tend to be more sensitive to the background wind filtering. Therefore, an additional assumption is needed to constrain the fitting by allowing the only solution for wave propagation directions to be opposite to the background wind. For the case in Figure 5b, the ill-fitted ring in Figure 5a will be eliminated by this additional constraint on the wave propagation direction.

In summary, the algorithm is able to run automatically and extract key wave properties, including location, amplitude, wavelength, and propagation direction for most of the GW events on a global basis. Since multiple CGW events rarely occur with similar amplitude in one image, the retrieved wavelength is unlikely to be overestimated, as indicated in Appendix B. It is also infrequent that the background wind and wave propagation are in the same direction in the AIRS image. The retrieval errors are negligible from the aforementioned assumptions (i.e., each image has a single GW event, and the wave propagation direction is opposite to the background zonal wind). The CGW patterns can be altered by a strong stratospheric wind shear. In this case, the vertical wavelength of the surviving half-rings not filtered out by critical-level filtering will be bent more vertically, resulting in more parallel wave structures. If this is the case (i.e., the so-called "wind skewing" effect), the ring center is closer to the wave front than the actual ring center, and the horizontal wavelength is overestimated (J. Alexander, personal communication, 2014).

3. Climatology of Ring Wave Parameters

There have been a few studies on individual CGW cases observed from AIRS and other instruments [e.g., *Yue et al.*, 2013]. Without specific wave classification, global GW climatology has also been studied extensively using AIRS radiances [e.g., *Hoffmann and Alexander*, 2009; *Gong et al.*, 2012; *Hoffmann et al.*, 2013], some of which focused on convectively generated GWs [e.g., *Hoffmann and Alexander*, 2010]. This study is aimed specifically at the ring type of GWs to produce the first global survey of these waves, as which is presented in the following two subsections.

3.1. Monthly Statistics of Ring Wave Parameters

CGWs are often associated with deep convection during the boreal summer in the NH, which is based on limited observations and case studies [e.g., *Yue et al.*, 2013]. From the AIRS global survey of CGWs, a significantly large number of nonplane wave events are found along the polar night jet in the winter hemisphere, as seen in Figure 2. We compiled two months' worth of AIRS observations to extract all ring events for January and July 2010, and the results for ring center location are shown in Figures 6 and 7. Ascending and descending orbits are separated to illustrate the diurnal differences in CGW properties.

In January, low-latitude ring events exhibit apparent association with tropical deep convection (indicated by thick black contours), while other ring events are found along the polar night jet and have larger amplitude,

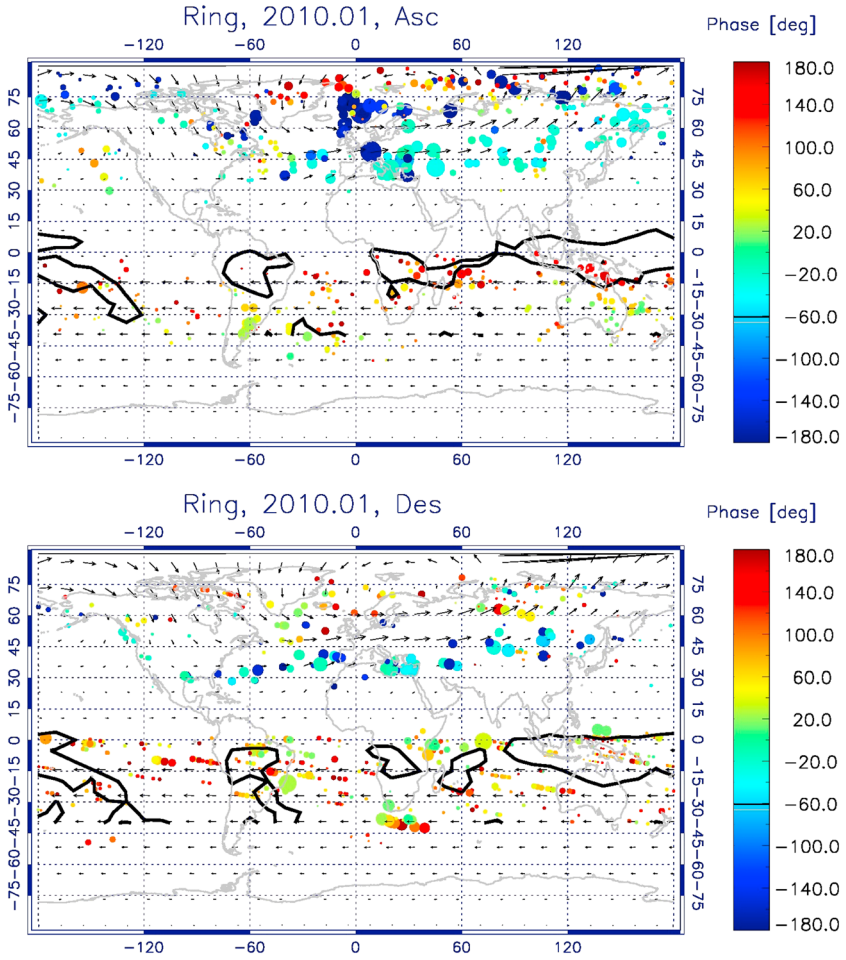

Figure 6. Geographic distribution of ring centers during January 2010 on (a) ascending and (b) descending orbits. The dot size is linearly proportional to wave amplitude, which varies from 1 to 5 K. Color corresponds to estimated phase propagation direction, with positive (negative) values meaning clockwise (counterclockwise) from the North. Arrows are MERRA monthly averaged wind vectors at 2.5 hPa. Thick black contours represent proxies of tropical deep convection (the same definition with that of *Wu and Eckermann* [2008]).

confirming the distribution seen in the daily map (Figure 2). The intensive deep convection in the tropics is highlighted using the monthly mean 215 hPa ice water content from the Microwave Limb Sounder (on the same A-Train orbit with AIRS) for values greater than 5 mg/m^3 [*Wu and Eckermann*, 2008]. In the tropics, ring wave centers tend to be located more over land during daytime (ascending) and more over the ocean during nighttime (descending). In the high-latitude winter hemisphere, ring waves are stronger during the local afternoon (ascending) than the local early morning (descending). The ring centers do not appear to collocate with topographic GW sources. Instead, they are spread along the polar night jet, suggesting importance of other sources, such as jet imbalance or convective fronts beneath the jet, and the effects of selective filtering by the background flow in the stratosphere.

Interestingly, the observed wave direction (color) manifests systematic toward-jet meridional phase propagation during daytime for both the easterly in the tropics and the westerly at high latitudes. The momentum flux direction is the same as the phase front propagation direction on the horizontal plane, indicating that concentric rings bring inward and backward momentum fluxes toward the jet, which effectively serves as a drag in the atmosphere at a high altitude. This meridional convergence feature was also found in a modeling study by *Sato et al.* [2012] at high latitudes and in the MLS observations by *Wu and Eckermann* [2008] in the tropics. However, such meridional preference in the CGW propagation becomes less significant or ambiguous to some extent during nighttime (Figure 6b).

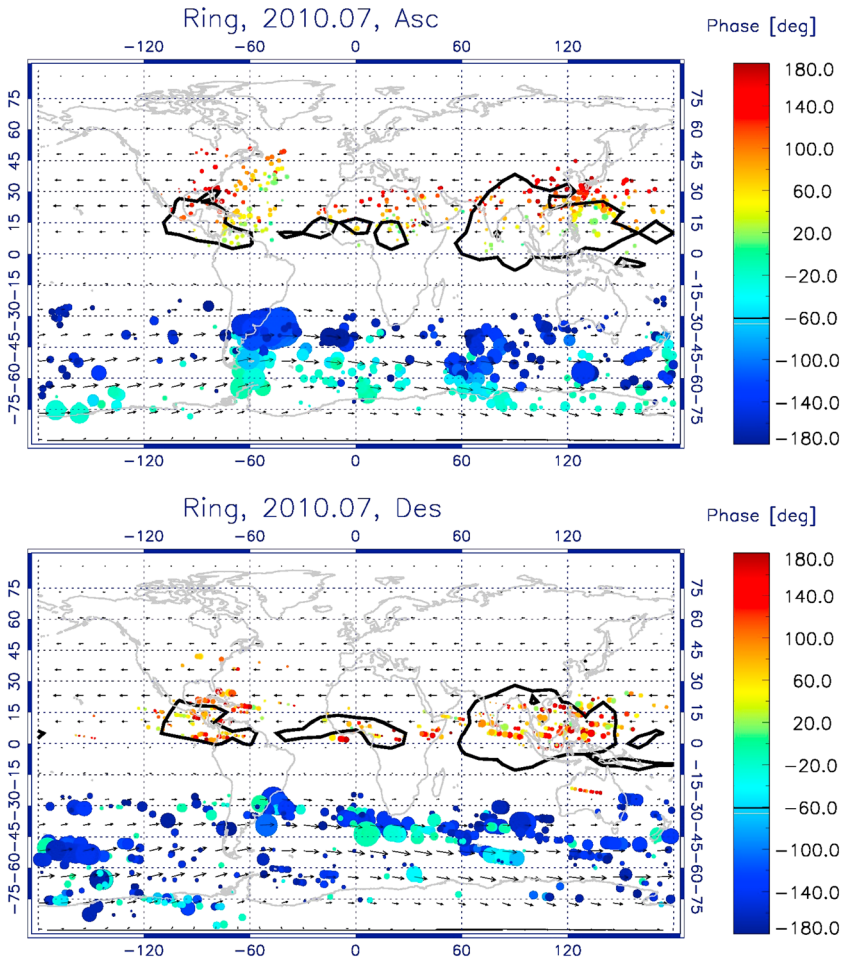

Figure 7. Same as Figure 6, except for July 2010.

In July, ring waves occur mostly to the north of tropical deep convection during daytime (Figure 7a) and along the polar night jet in the SH. The latitudinal distribution of preferred meridional propagation direction is more pronounced than it is in January, implying a stronger momentum drag to the westerly and easterly jets in the upper atmosphere. At night (Figure 7b), the center of tropical ring waves moves to the south slightly and collocates better with tropical deep convection. *Jiang et al*. [2004b] and *Wu and Eckermann* [2008] also reported poleward shifts of convective GW activities with respect to tropical deep convections, which were attributed to the meridional wind-filtering effect. As such a poleward shift is not apparent during nighttime in our result, the meridional structure of the GW source spectrum may play an important role in explaining such a diurnal disparity. High-latitude ring waves usually have larger amplitude than tropical ones. The most vigorous ring events at high latitudes seem associated with islands in the Southern Ocean, such as South Georgia Island, Marion Island, Possession Island, South Sandwich Island, Kerguelen Island, and New Zealand. However, ring waves are also frequently identified over the Andes and Antarctic Peninsula during daytime (Figure 7a), but not nighttime. These events may be spuriously classified as rings due to the interference of topographic GWs generated by the aforementioned two topographic sources. The preference of jet-inward meridional propagation disappears in the July nighttime observation.

Diurnal variations in the ring wave location, amplitude, and phase propagation direction have not been reported in literature, and we attempt here to point out this local time dependence. Because the 2.5 hPa mean wind has little diurnal variations, the observed diurnal variations in CGW properties must be associated with diurnally varying GW sources and/or the flows at altitudes below 2.5 hPa. For example, tropical deep convection is the strongest over land in the late afternoon, while oceanic convection is stronger during late

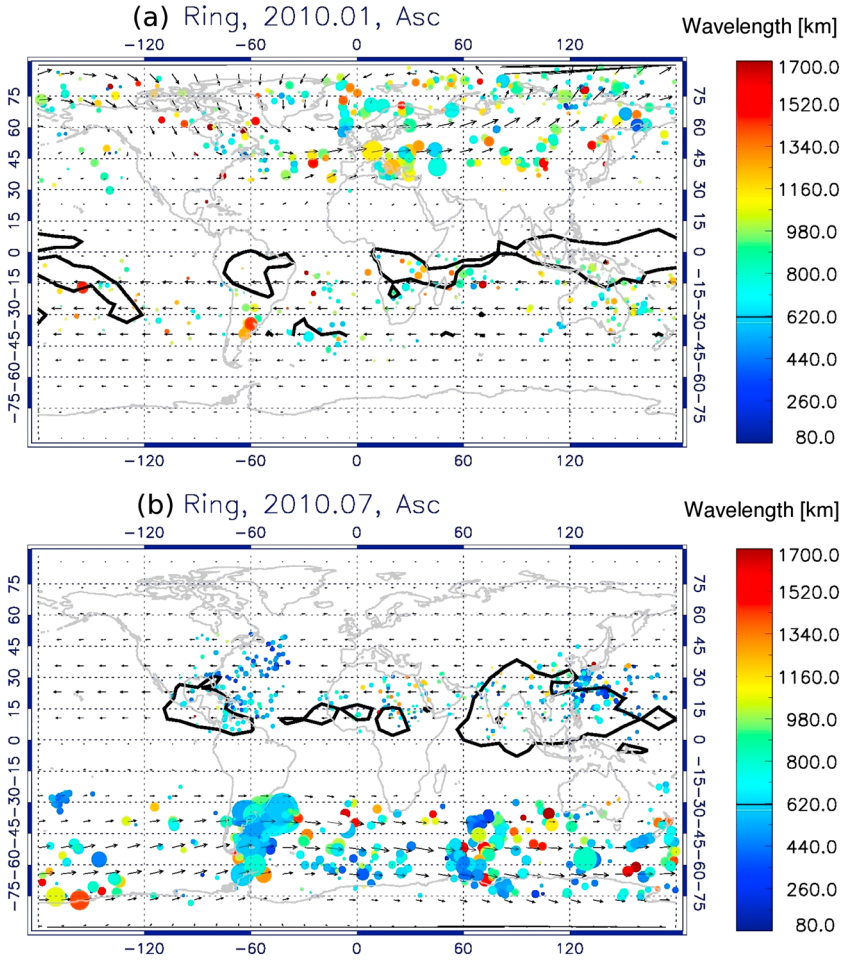

Figure 8. Horizontal wavelength (color) for ring waves occurring in (a) January and (b) July 2010 for ascending orbits only. Since no day-night contrast has been found for this variable, results from descending orbits are not shown. Symbol size and contours correspond with those in Figure 6.

night–early morning [*Tian et al.*, 2004]. Hence, it is plausible that the locations of tropical ring events follow the lifecycle of deep convection. However, there is no indication that the convective ring wave strength has a diurnal cycle. This may be caused by the fact that AIRS equator passing time (1:30 A.M. and P.M.) misses the diurnal peak and trough of tropical deep convections or maybe that AIRS's observational geometry limits the sensitivity to the dramatic change of convective GW spectrum. In July, the United States east coast and China are the two hotspots of convective concentric rings, especially during daytime. Hurricanes and typhoons may be the possible corresponding sources. These two regions were also previously reported to have the most frequent convective overshooting events [*Anderson et al.*, 2012]. *Hoffman et al.* [2013] reported NH midlatitude summer GW hotspots over the continental U.S. and Southeastern China. The "wind skewing" effect may be another explanation of the coastal hotspots identified here. The upper level westerly in midlatitude summer provides a favorable condition for concentric ring waves to propagate upward, whereas the diurnally varying convective source over land could be another source for these hotspots during daytime [*Hoffmann and Alexander*, 2010]. Ring centers off the coasts may be due to the "wind skewing" effect as mentioned in the previous section because deep convections are more likely to occur over land than over the ocean in the midlatitudes. In other words, the actual ring centers should be located to the west of the identified ones (i.e., central or eastern US), which is consistent with previous case studies [*Yue et al.*, 2013]. This effect may also account for the frequent daytime occurrence of ring waves over the Sahara in July. At high latitudes, the geographic distribution of ring centers suggests the extratropical jet as a major wave source, such as jet imbalance or frontal/convective systems from vigorous winter storms. As the geographic location is not apparently along the NH storm tracks during boreal winter (Figure 6), the polar night jet is another

possible source for these ring waves [*Yamashita et al*., 2010]. In the SH, interestingly, large-amplitude ring waves often occur near isolated islands in the austral winter, which is an effective-but-missing wave excitation mechanism as suggested in *Alexander and Grimsdell* [2013]. Since islands can be considered as a point source, a strong tropospheric flow could introduce wake-like GW structures around them [*Alexander and Grimsdell*, 2013]. Downstream from the islands, the wake curvature could be identified as a ring wave by our method. These are not "concentric rings," strictly speaking, but instead are GWs with "ring-like" morphology. It is not clear what causes the day-night difference in the latitudinal preference of wave propagation in the meridional direction. GW-tidal wave interactions in the upper troposphere/lower stratosphere region and/or diurnally varying deep convective GW sources are among the plausible causes.

Little day-night differences are found in the CGW horizontal wavelength, and therefore, only ascending results are shown in Figure 8. The majority of the ring wavelengths fall between 400 and 1300 km, as expected for mesoscale internal GWs. The wavelength range is limited by AIRS footprint size and swath width as well. No significant differences exist between wavelengths in the tropics and at high latitudes, nor any significant longitudinal variations. The average CGW wavelength in January (800 km) is ~300 km longer than that in July (500 km). Studies of the global Mesoscale Convective Complex (MCC) showed no distinct difference in the size between the NH and SH [*Laing and Fritsch*, 1997], which contradicts the linear CGW generation theory that the GW horizontal wavelength is proportional to the dimension of the heating source [*Beres et al*., 2004]. Note that the ring wave morphology is affected by both wave source characteristics and the background wind between the wave generation level and 2.5 hPa. Hence, the stratospheric background wind differences between January and July may cause the hemispheric contrast of horizontal wavelength. According to the GW dispersion relationship, horizontal wavenumber k can be expressed as

$$k = \frac{fm}{N^2}\frac{\overline{\partial V_n}}{\partial z} \pm \frac{m}{N}\left[\frac{f^2}{N^2}\frac{\overline{\partial V_n}^2}{\partial z} + \omega^2 - f^2\right]^{\frac{1}{2}} \quad (1)$$

where f is the Coriolis parameter, N is the Brunt-Väisälä frequency, m is the vertical wavenumber, ω is the GW frequency, and V_n is the horizontal background wind perpendicular to the direction of wave propagation. Equation (1) neglects the density scale height term, and k takes positive values at the direction of phase front propagation [*Hankinson et al*., 2014a, 2014b]. Therefore, k increases (i.e., horizontal wavelength decreases) with the vertical wind shear. This wave dispersion property is confirmed by model simulations [*Alexander et al*., 2006], which can explain the horizontal wavelength difference between January and July since the polar night jet strength is weaker in boreal winter (January). This mechanism does not explain the interhemispheric wavelength difference in the summer easterly regions. *Laing and Fritsch* [1997] showed that the most probable MCC size was ~300 km for both hemispheres, but the size spectrum was broader in the SH with most power coming from 400 to 700 km MCCs, which possibly explaining the CGW wavelength discrepancy in the tropics. Moreover, the observed CGW wavelengths are consistent with the study in *Beres et al*. [2004], approximately twice the size of their convective sources. These are resolvable scales in the ECMWF T1279 analysis, but how well are the modeled waves compared to those observed by AIRS?

3.2. Comparison Between AIRS and ECMWF-Resolved Concentric Ring Properties

Although ECMWF-resolved GWs resemble AIRS daily observations quite well (Figure 2), there are some critical differences in the wave parameters. Figures 9 and 10 compare latitudinal variations of wavelength, axial ratio (λ_y/λ_x, where λ is the horizontal wavelength), phase propagation direction, amplitude, and number of events during January and July 2010. Although the number of events does not correspond to the actual wave intermittency because of subsampling and possible over counting, it is still meaningful to this task as AIRS spatial and temporal sampling is applied to ECMWF data prior to the CGW analysis.

For ring wave wavelength and shape represented by the axial ratio parameter, ECMWF can reproduce these waves throughout all latitudes, particularly during daytime (i.e., ascending orbit). Both ECWMF and AIRS capture the monotonic dominant wavelength mode at ~800 km during January and ~500 km during July. The characteristic wavelengths are similar in the wave spectra of unfiltered ECMWF data (not shown), suggesting that they are a real wave property for these months, rather than view-geometry preference. Overall, concentric rings in ECMWF are slightly skinnier than those observed by AIRS, as the axial ratio is overestimated in ECMWF.

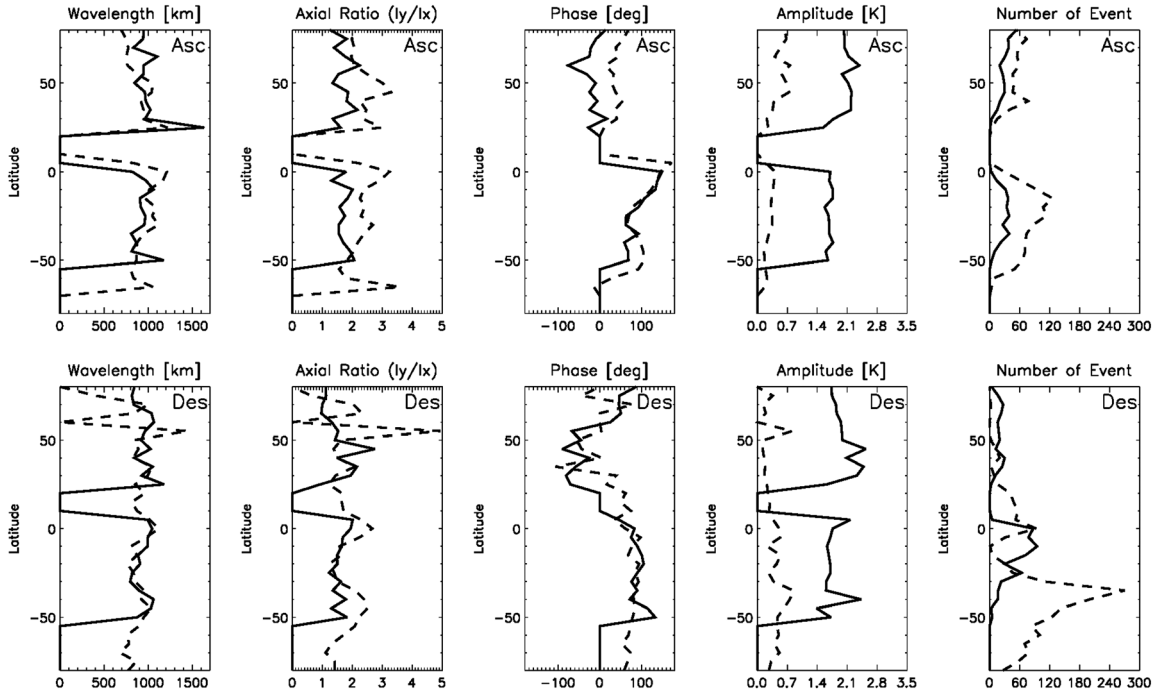

Figure 9. Latitudinal variation of mean wavelength (first column), axial ratio ($\lambda y/\lambda x$, second column), phase propagation direction (third column), amplitude (fourth column), and number of events (fifth column). The black solid (dashed) line is from AIRS (ECMWF) for January 2010. (top) Ascending and (bottom) descending orbits.

For the wave phase propagation direction, ECMWF is able to produce the jet-inward propagation as observed during daytime in both months. In the winter hemisphere, the ECMWF analysis mimics the AIRS-observed CGWs, but the wave geographic distributions are different (Figures 11 and 12). For example, in July, most of the large-amplitude rings occur over the tips of Andes and Antarctic Peninsula, as well as over the islands in

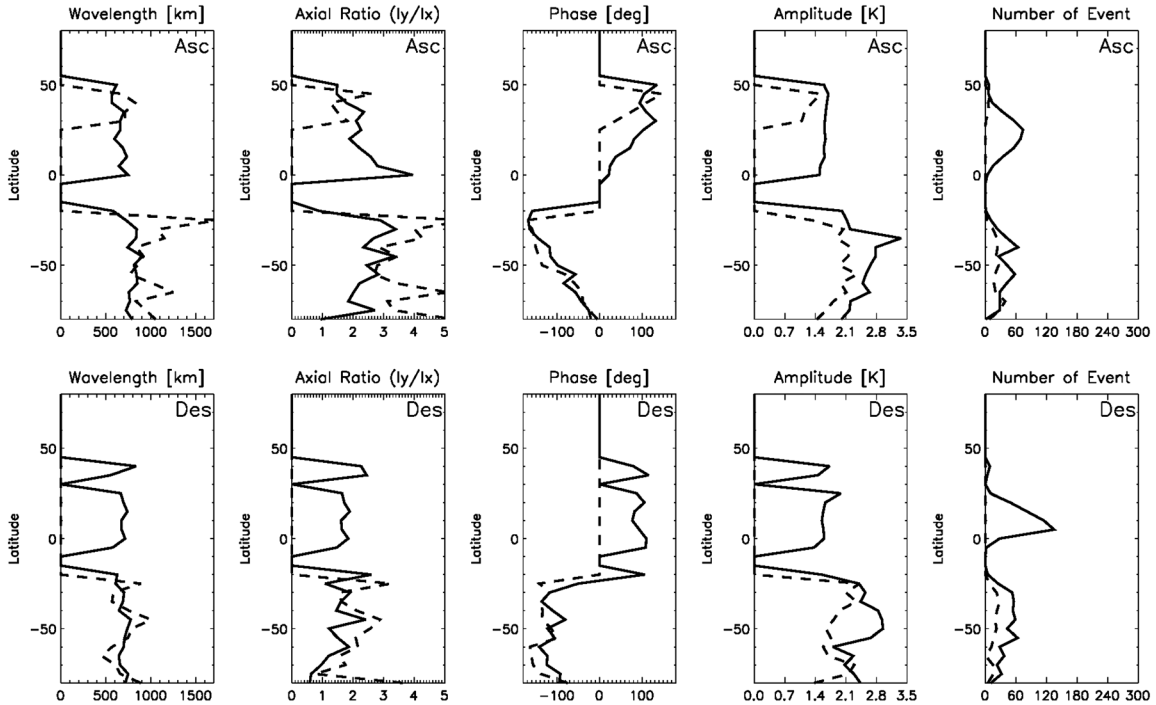

Figure 10. Same as Figure 9, but for July 2010.

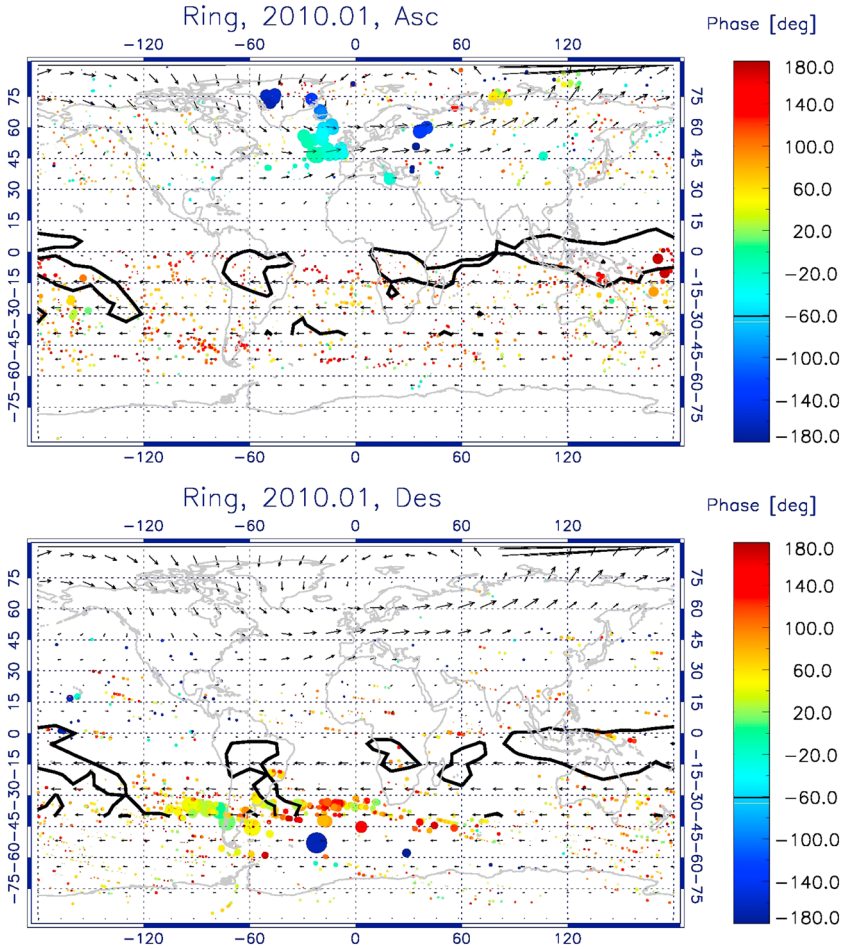

Figure 11. Same as Figure 6, except for ECMWF-resolved rings during January 2010. The wave amplitude range is changed to 0.5–2.5 K (half of the range of Figure 6).

the Southern Ocean during daytime. Topography seems to play a more important role in ECMWF. However, ring waves in the NH occur almost everywhere along the jet during January in the AIRS observation (Figure 6) but only occur during daytime in the Atlantic branch of the jet stream in ECMWF. This introduces a net positive phase propagation direction in ECMWF at mid-high latitudes during January where the wave phase front should mostly propagate westward as seen by AIRS. In the summer hemisphere, ECMWF results compare better with the observations for January than for July because a great number of convective concentric rings are unresolved by the ECMWF analysis (e.g., Eastern China).

Wave amplitude, as described above, is significantly underestimated in ECMWF in January. However, the average wave amplitude increased after the model horizontal resolution was improved from 25 to 16 km at the end of January 2010. Compared to less than 20% of AIRS wave amplitude in January, ECMWF improves to ~70% of the observed amplitude in July. However, increasing model resolution does not improve convectively generated concentric rings very much. In fact, merely any convective rings can be identified during July in the summer hemisphere (Figure 12). Because the wave amplitude in January is weak, an excessive amount of ring waves was then generated to partly offset such a discrepancy (Figure 9, last column). As the model resolution increases, the wave occurrence frequency decreases, along with the increase of wave amplitude. However, the wave amplitude weighted wave occurrence frequency remains too small (approximately one third) compared to what is observed in AIRS.

All in all, the ECMWF-resolved ring waves are generally similar to the AIRS observations in terms of wavelength, shape, and propagation direction. However, the ECMWF wave amplitude is too weak and is unable to produce convectively generated CGWs in NH summer. With the increased model resolution, the

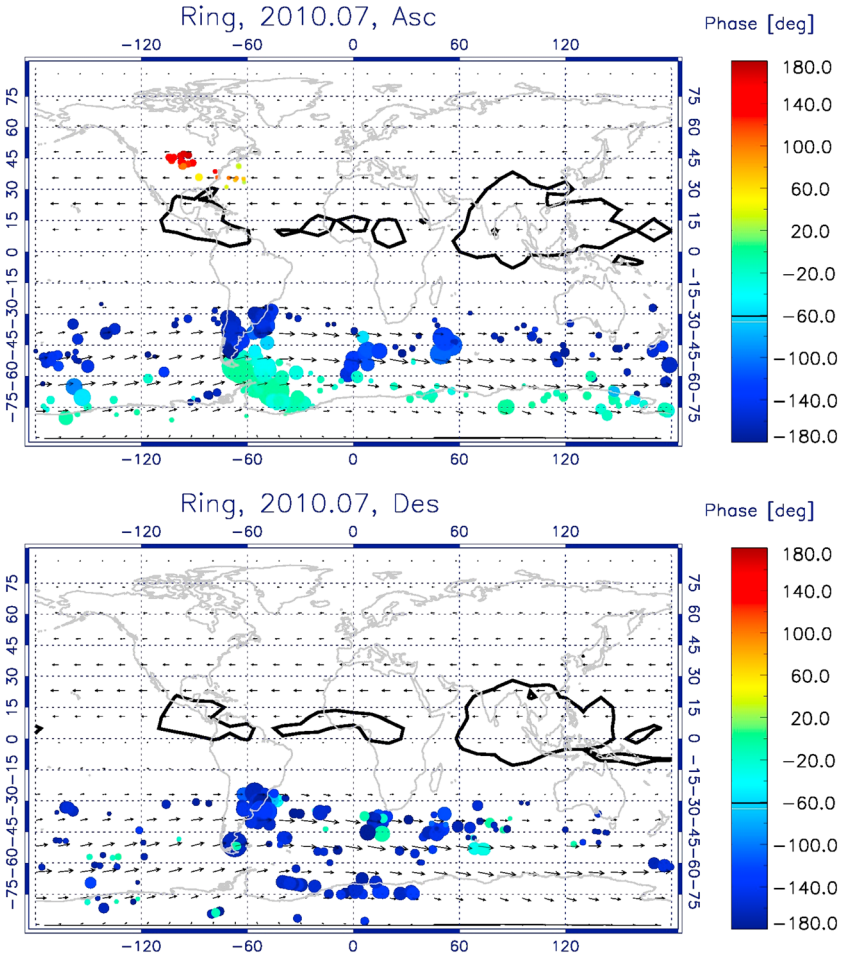

Figure 12. Same as Figure 11, except for July 2010.

wave amplitude is greatly improved (from 30% to 70% with respect to the observed amplitude on average), while the wave occurrence frequency significantly deceases. Because noise in the ECMWF data is effectively 0, the detection threshold may be loosened. *Preusse et al.* [2014] reported that horizontal wavelengths of the resolved GWs in ECMWF are longer than the observation. Since they used data from limb instruments (SABER) and included all types of GWs for comparisons, the results therein are not directly comparable to this study.

In order to correctly model general circulation in the middle and upper atmosphere, the amount of GWD exerted on the mean flow needs to take into account the model resolution. Since the resolved ring waves are too weak, their contribution to GWD needs to be compensated by GWD parameterization in the model. There must have been an excessive amount of unresolved GWs that are currently parameterized in ECMWF. Consequently, the skewed GW spectrum is likely one of the major causes of model biases in the middle and upper atmosphere [*Geller et al.*, 2013].

4. Conclusions

A novel ring-pattern detection algorithm is developed here and applied successfully to the AIRS radiance data and ECMWF analysis data to extract CGWs or partial CGWs. The unique "L-shape" power distribution in the two-dimensional (2-D) Fourier spectrum provides a distinguishable feature to separate between ring waves and plane GWs. The algorithm produces robust detection of ring patterns and can be readily modified for processing data from other channels or imagers.

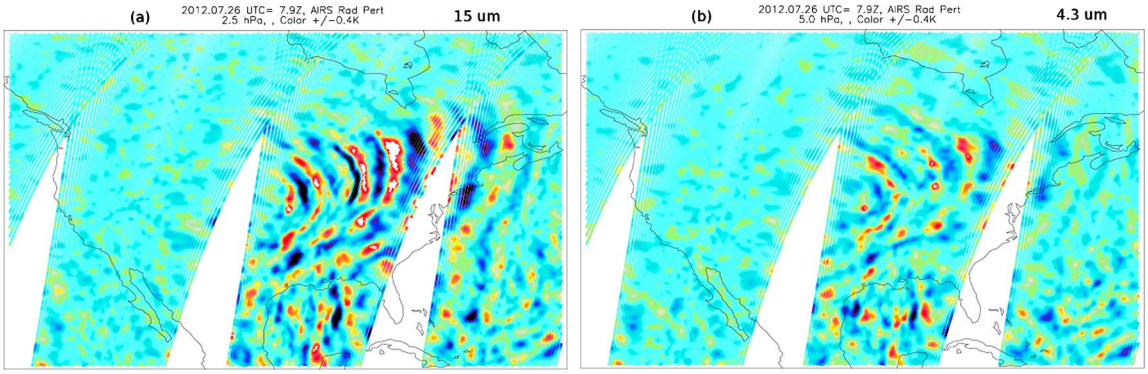

Figure A1. Same as Figure 1a, except that (b) is from a subset of 4.3 μm channels. The channel numbers for generating Figure A1b are 2055, 2056, 2062, 2076, 2082, 2084, 2087-2089, and2092-2101.

Two months of AIRS brightness temperature data were analyzed to produce the first global survey of CGWs at 2.5 hPa. We found that the ring waves are mostly associated with the tropical and subtropical deep convection in summer, and extratropical jet imbalance and/or embedded fronts and convection in winter. In July, the islands in the Southern Ocean appear to be an additional source of CGWs. The jet and island sources are different from the conventional view of ring wave sources. There is a strong diurnal difference in geographical distribution of ring wave occurrence and phase propagation. The ring waves have preference to propagate upward into the winter polar westerly jet and into the summer subtropical easterly jet during daytime. This preferential propagation is not observed in the nighttime data, which implies a stronger CGW momentum forcing during daytime. The diurnal variation of deep convection is a plausible cause but other possibilities warrant future investigations. Instead of the diurnal variation, the CGW wavelength and wave amplitude also exhibit seasonal variations. CGWs have a longer wavelength and weaker amplitude in January (1000 km, 2 K) compared to July (800 km, 2.8 K).

The ring detection algorithm is also applied to the ECMWF analysis data. Since the CGWs in the analysis data are mostly generated by the underlying GCM, comparisons with AIRS observations provide a valuable diagnosis of model-resolved GWs. To ensure the comparability in wave observations, the AIRS observational filters (spatial sampling and weighting function) are applied to ECMWF analysis data before extracting the ring waves. We find that the ECMWF model can produce the concentric CGWs similar to the AIRS observations. The CGW properties in the T1261 analysis resemble most of the AIRS observations. However, the convectively generated CGWs are still lacking in the ECMWF analysis. Since deep convection often occurs at scales shorter than 16 km and needs to be parameterized in GCMs, it is not surprising to find this wave source is underestimated. It will remain as a major challenge for GCMs to properly represent convectively generated GWs and their impacts on troposphere-stratosphere exchange of trace gases, water vapor and aerosols.

Appendix A: Pros and Cons of 15 μm and 4.3 μm Channels

Hoffmann and Alexander [2009, 2010] suggested that AIRS 4.3 μm CO_2 channels are a great choice for studying convective GWs, as these channels have 2–5 times more radiance response than 15 μm channels under the same atmospheric condition. We also found that 4.3 μm channels were good for observing concentric rings. However, the noise level for 4.3 μm channels is also at least 2 times that of the 15 μm channels in general [*Hoffmann and Alexander*, 2009]. This means we need to add multiple 4.3 μm channels together to average down the noise, and the GW signal is also smoothed out substantially. This can be easily seen from Figure A1b compared with Figure A1a. More importantly, 4.3 μm channels have a much broader WF width (>21 km), meaning that they lack the capability of discerning GWs with vertical wavelength ranging between 12 and 21 km and above. Previous modeling and observational works suggested that one third to one half of the stratospheric and mesospheric GW variances were from GWs of vertical wavelength between 10 and 20 km [*Krebsbach and Preusse*, 2007; *Choi et al.*, 2012]. Using 4.3 μm channels may potentially overlook a great portion of GWs that carry significant amount of momentum fluxes. Non-LTE effects present at 4.3 μm channels during daytime cause occasional failure of retrieving GW information [*Strow et al.*, 2006].

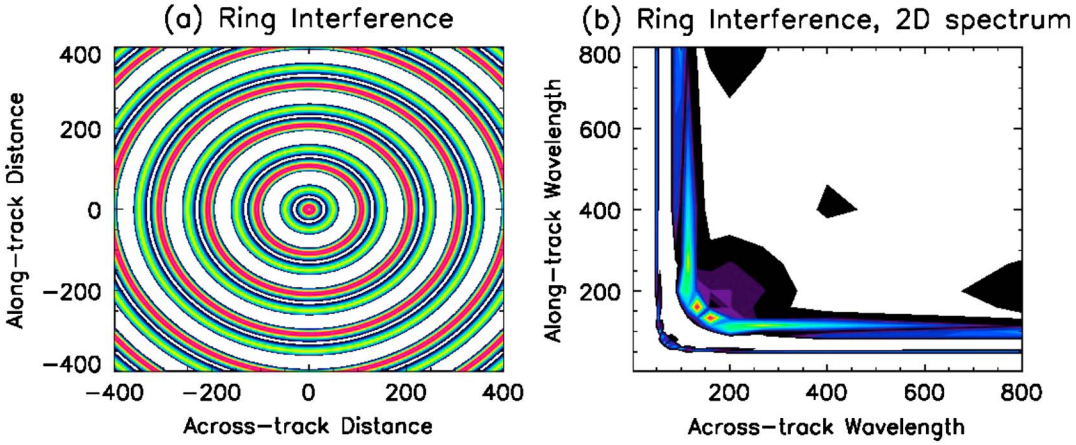

Figure B1. Same meaning as Figure 3, except two concentric rings with the same center and different wavelengths are superimposed onto each other.

Having stated above the advantages of using 15 μm band, we nevertheless did conduct some preliminary comparisons between daily ring maps from these two frequency bands. During the summer in the Continental United States for example, some westward propagating half-ring features can be identified on 4.3 μm maps but not on 15 μm maps. Wave amplitudes are not necessarily smaller in 4.3 μm maps either (not shown). Broader WFs for 4.3 μm channels apparently cause some of the differences, but the details are out of the scope of this research. Therefore, 4.3 and 15 μm channels work well as compliments to each other. The present ring detection technology is by all means applicable to 4.3 μm images as well.

Appendix B: Details of Idealized Wave Functions and Wave Interference Situation

The idealized wave function for sinusoidal wave shown in Figure 3a is

$$Amp = \cos\left(\frac{2\pi(x-x_0)}{\lambda_x}\right)e^{-\left(x-x_0/2x_{\max}\right)^2/2}\cdot\cos\left(\frac{2\pi(y-y_0)}{\lambda_y}\right)e^{\frac{-\left(y-y_0/2y_{\max}\right)^2}{2}} \tag{B1}$$

where Amp is the wave amplitude, λ_x (λ_y) is the cross-track (along-track) wavelength, and $x_{\max}$ ($y_{\max}$) is the cross-track (along-track) frame width divided by 2.

For a plane wave, the expression is

$$Amp = \cos\left(\frac{2\pi(x-x_0)}{\lambda_x}+\frac{2\pi(y-y_0)}{\lambda_y}\right) \tag{B2}$$

For a concentric ring, the expression is

$$Amp = \cos\left(\frac{2\pi\left(R-\sqrt{\lambda_y^2(x-x_0)^2+\lambda_x^2(y-y_0)^2}\right)}{\lambda_x\lambda_y}\right) \tag{B3}$$

where x_0 (y_0) stands for the ring center along cross-track (along-track) direction. Values of $\lambda_x = 150$ and $\lambda_y = 200$ were used to compose Figure 3.

However, in the situation when two ring waves with similar amplitudes are superimposed on top of each other, the strong wave interference forms the new "wave packet," whose wavelength is different from either of the original ones. In Figure B1a, one wave has $\lambda_x = \lambda_y = 200$, and the other is $\lambda_x = \lambda_y = 100$. The largest power at the corner of the broader "L-shape" in Figure B1b corresponds to $\lambda_x = \lambda_y = 150$, while the other sharper "L-shape" has a corner at $\lambda_x = \lambda_y = 50$.

The current paper assumes such a situation would not occur in nature.

Acknowledgments
This work is performed at the NASA Goddard Space Flight Center with support from the NASA NNH10ZDA001N-ESDRERR (Earth System Data Records Uncertainty Analysis) project. J. Y. is supported by NASA NNX14AF20G and NNH13ZDA001N-HGI. We are grateful to the AIRS team at Jet Propulsion Lab and NASA DISC in providing the AIRS brightness temperature and the ECMWF analysis data, to J. Alexander and L. Grasso for useful discussions, and to Megan Buzanowicz of Hampton University and Christina Bromley of George Washington Online High School for final proofreading. Comments and suggestions from J. Jiang and another anonymous reviewer are highly acknowledged. The data and algorithm codes are available upon request by sending an email to Jie.Gong@nasa.gov.

References

Alexander, M. J., and A. W. Grimsdell (2013), Seasonal cycle of orographic gravity wave occurrence above small islands in the Southern Hemisphere: Implications for effects on the general circulation, *J. Geophys. Res. Atmos.*, *118*, 11,589–11,599, doi:10.1002/2013JD020526.

Alexander, M. J., J. Richter, and B. R. Sutherland (2006), Generation and trapping of gravity waves from convection with comparison to parameterization, *J. Atmos. Sci.*, *63*, 2963–2977, doi:10.1175/JAS3792.1.

Anderson, J. G., D. M. Wilmouth, J. B. Smith, and D. S. Sayres (2012), UV dosage levels in summer: Increased risk of ozone loss from convectively injected water vapor, *Science*, *337*, 835.

Beres, J. H. (2004), Gravity wave generation by a three-dimensional thermal forcing, *J. Atmos. Sci.*, *61*, 1805–1815.

Choi, H.-J., H.-Y. Chun, J. Gong, and D. L. Wu (2012), Comparison of gravity wave temperature variances from ray-based spectral parameterization of convective gravity wave drag with AIRS observations, *J. Geophys. Res.*, *117*, D05115, doi:10.1029/2011JD016900.

Dewan, E. M., R. H. Picard, R. R. O'Neil, H. A. Gardiner, J. Gibson, J. D. Mill, E. Richards, M. Kendra, and W. O. Gallery (1998), MSX satellite observations of thunderstorm-generated gravity waves in mid-wave infrared images of the upper stratosphere, *Geophys. Res. Lett.*, *25*(7), 939–942, doi:10.1029/98GL00640.

Eckerman, S. D., J. Ma, D. L. Wu, and D. Broutman (2007), A three dimensional mountain wave imaged in satellite radiance throughout the stratosphere: Evidence of the effects of directional wind shear, *Q. J. R. Meteorol. Soc.*, *133*(629), 1959–1975.

Fritts, D. C., and M. J. Alexander (2003), Gravity wave dynamics and effects in the middle atmosphere, *Rev. Geophys.*, *41*(1), 1003, doi:10.1029/2001RG000106.

Fritts, D. C., et al. (2008), Gravity wave and tidal influences on equatorial spread F based on observations during the Spread F Experiment (SpreadFEx), *Ann. Geophys.*, *26*, 3235–3252.

Geller, M. A., et al. (2013), A comparison between gravity wave momentum fluxes in observations and climate models, *J. Clim.*, *26*, 6383–6405, doi:10.1175/JCLI-D-12-00545.1.

Gong, J., and D. L. Wu (2014), CloudSat-constrained cloud ice water path and cloud top height retrievals from MHS 157 and 183.3 GHz radiances, *Atmos. Meas. Tech.*, *7*, 1873–1890.

Gong, J., D. L. Wu, and S. D. Eckermann (2012), Gravity wave variances and propagation derived from AIRS radiances, *Atmos. Chem. Phys.*, *12*(4), 1701–1720.

Grimsdell, A. W., M. J. Alexander, P. T. May, and L. Hoffmann (2010), Model study of waves generated by convection with direct validation via satellite, *J. Atmos. Sci.*, *67*, 1617–1631.

Hankinson, M. C. N., M. J. Reeder, and T. P. Lane (2014a), Gravity waves generated by convection during TWP-ICE: 1. Inertia-gravity waves, *J. Geophys. Res. Atmos.*, *119*, 5269–5282, doi:10.1002/2013JD020724.

Hankinson, M. C. N., M. J. Reeder, and T. P. Lane (2014b), Gravity waves generated by convection during TWP-ICE: 2. High-frequency gravity waves, *J. Geophys. Res. Atmos.*, *119*, 5257–5268, doi:10.1002/2013JD020726.

Hines, C. O. (1960), Internal atmospheric gravity waves at ionospheric heights, *Can. J. Phys.*, *38*, 1441.

Hines, C. O. (1988), Generation of turbulence by atmospheric gravity waves, *J. Atmos. Sci.*, *45*, 1269–1278.

Hoffmann, L., and M. J. Alexander (2009), Retrieval of stratospheric temperatures from Atmospheric Infrared Sounder radiance measurements for gravity wave studies, *J. Geophys. Res.*, *114*, D07105, doi:10.1029/2008JD011241.

Hoffmann, L., and M. J. Alexander (2010), Occurrence frequency of convective gravity waves during the North American thunderstorm season, *J. Geophys. Res.*, *115*, D20111, doi:10.1029/2010JD014401.

Hoffmann, L., X. Xue, and M. J. Alexander (2013), A global view of stratospheric gravity wave hotspots located with Atmospheric Infrared Sounder observations, *J. Geophys. Res. Atmos.*, *118*, 416-434, doi:10.1029/2012JD018658,.

Hoffmann, L., M. J. Alexander, C. Clerbaux, A. W. Grimsdell, C. I. Meyer, T. Rößler, and B. Tournier (2014), Intercomparison of stratospheric gravity wave observations with AIRS and IASI, *Atmos. Meas. Tech. Discuss.*, *7*, 8415–8464.

Jiang, J. H., and D. L. Wu (2001), UARS MLS observations of gravity waves associated with the Arctic Winter Stratospheric Vortex, *Geophys. Res. Lett.*, *28*, 527–530, doi:10.1029/2000GL011800.

Jiang, J. H., D. L. Wu, S. D. Eckermann, and J. Ma (2003), Mountain waves in the middle atmosphere: Microwave limb sounder observations and analyses, *Adv. Space Res.*, *32*(5), 801–806.

Jiang, J. H., S. D. Eckermann, D. L. Wu, and J. Ma (2004a), A search for mountain waves in MLS stratospheric limb radiances from the winter Northern Hemisphere: Data analysis and global mountain wave modeling, *J. Geophys. Res.*, *109*, D03107, doi:10.1029/2003JD003974.

Jiang, J. H., B. Wang, K. Goya, K. Hocke, S. D. Eckermann, J. Ma, D. L. Wu, and W. G. Read (2004b), Geographical distribution and inter-seasonal variability of tropical deep-convection: UARS MLS observations and analyses, *J. Geophys. Res.*, *109*, D03111, doi:10.1029/2003JD003756.

Kim, S.-Y., and H.-Y. Chun (2011), Impact of typhoon-generated gravity waves in the typhoon development, *Geophys. Res. Lett.*, *38*, L01806, doi:10.1029/2010GL045719.

Krall, J., J. D. Huba, and D. C. Fritts (2013), On the seeding of equatorial spread F by gravity waves, *Geophys. Res. Letts.*, *40*, 661–664, doi:10.1002/grl.50144.

Laing, A. G., and J. M. Fritsch (1997), The global population of mesoscale convective complexes, *Q. J. R. Meteorol. Soc.*, *123*, 389–405.

Lilly, D. K. (1978), A severe downslope windstorm and aircraft turbulence event induced by a mountain wave, *J. Atmos. Sci.*, *35*, 59–77.

Mapes, B. E. (1993), Gregarious tropical convection, *J. Atmos. Sci.*, *50*, 2026–2037.

Miller, S. D., S. P. Mills, C. D. Elvidge, D. T. Lindsey, T. F. Lee, and J. D. Hawkins (2012), Suomi satellite brings to light a unique frontier of nighttime environmental sensing capabilities, *Proc. Natl. Acad. Sci. U.S.A.*, *109*, 39, doi:10.1073/pnas.1207034109.

Nishioka, M., T. Tsugawa, M. Kubota, and M. Ishii (2013), Concentric waves and short-period oscillations observed in the ionosphere after the 2013 Moore EF5 tornado, *Geophys. Res. Lett.*, *40*, 5581–5586, doi:10.1002/2013GL057963.

Plougonven, R., and F. Zhang (2014), Internal gravity waves from atmospheric jets and fronts, *Rev. Geophys.*, *52*, 33–76, doi:10.1002/2012RG000419.

Preusse, P., M. Ern, P. Bechtold, S. D. Eckermann, S. Kalisch, Q. T. Trinh, and M. Riese (2014), Characteristics of gravity waves resolved by ECMWF, *Atmos. Chem. Phys.*, *14*, 10,483–10,508, doi:10.5194/acp-14-10483-2014.

Richter, J. H., F. Sassi, and R. R. Garcia (2010), Toward a physically based gravity wave source parameterization in a general circulation model, *J. Atmos. Sci.*, *67*, 136–156.

Sato, K., S. Tateno, S. Watanabe, and Y. Kawatani (2012), Gravity wave characteristics in the Southern Hemisphere revealed by a high-resolution middle-atmosphere general circulation model, *J. Atmos. Sci.*, *69*, 1378–1396.

Schroeder, S., P. Preusse, M. Ern, and M. Riese (2009), Gravity waves resolved in ECMWF and measured by SABER, *Geophys. Res. Lett.*, *36*, L10805, doi:10.1029/2008GL037054.

Sentman, D. D., et al. (2003), Simultaneous observations of mesospheric gravity waves and sprites generated by a midwestern thunderstorm, *J. Atmos. Sol. Terr. Phys.*, *65*, 537–550, doi:10.1016/S1364-6826(02)00328-0.

Smith, S., J. Baumgardner, and M. Mendillo (2009), Evidence of mesospheric gravity waves generated by orographic forcing in the troposphere, *Geophys. Res. Lett.*, *36*, L08807, doi:10.1029/2008GL036936.

Strow, L. L., S. E. Hannon, S. De-Souza Machado, H. E. Motteler, and D. C. Tobin (2006), Validation of the Atmospheric Infrared Sounder radiative transfer algorithm, *J. Geophys. Res.*, *111*, D09S06, doi:10.1029/2005JD006146.

Suzuki, S., K. Shiokawa, Y. Otsuka, T. Ogawa, K. Nakamura, and T. Nakamura (2007), A concentric gravity wave structure in the mesospheric airglow images, *J. Geophys. Res.*, *112*, D02102, doi:10.1029/2005JD006558.

Taylor, M. J., and M. A. Haphood (1988), Identification of a thunderstorm as a source of short period gravity waves in the upper atmospheric nightglow emissions, *Planet Space Sci.*, *36*(4), 975–985.

Tian, B., B. J. Soden, and X. Wu (2004), Diurnal cycle of convection, clouds and water vapor in the tropical upper troposphere: Satellites versus a general circulation model, *J. Geophys. Res.*, *109*, D10101, doi:10.1029/2003JD004117.

Tsugawa, T., A. Saito, Y. Otsuka, M. Nishioka, T. Maruyama, H. Kato, T. Nagatsuma, and K. T. Murata (2011), Ionospheric disturbances detected by GPS total electron content observation after the 2011 off the Pacific coast of Tohoku Earthquake, *Earth Planets Space*, *63*, 875–879.

Vadas, S. L., and H.-L. Liu (2009), The generation of large-scale gravity waves and neutral winds in the thermosphere from the dissipation of convectively-generated gravity waves, *J. Geophys. Res.*, *114*, A10310, doi:10.1029/2009JA014108.

Wu, D. L., and S. D. Eckermann (2008), Global gravity wave variances from Aura MLS: Characteristics and interpretation, *J. Atmos. Sci.*, *65*, 3695–3718.

Wu, D. L., P. Preusse, S. D. Eckermann, J. H. Jiang, M. T. Juarez, L. Coy, and D. Y. Wang (2006), Remote sounding of atmospheric gravity waves with satellite limb and nadir techniques, *Adv. Space Res.*, *37*, 2269–2277.

Yamashita, C., H.-L. Liu, and X. Chu (2010), Gravity wave variations during the 2009 stratospheric sudden warming as revealed by ECMWF-T799 and observations, *Geophys. Res. Lett.*, *37*, L22806, doi:10.1029/2010GL045437.

Yue, J., S. L. Vadas, C.-Y. She, T. Nakamura, S. C. Reising, H.-L. Liu, P. Stamus, D. A. Krueger, W. Lyons, and T. Li (2009), Concentric gravity waves in the mesosphere generated by deep convective plumes in the lower atmosphere near Fort Collins, Colorado, *J. Geophys. Res.*, *114*, D06104, doi:10.1029/2008JD011244.

Yue, J., L. Hoffmann, and M. J. Alexander (2013), Simultaneous observations of convective gravity waves from a ground-based airglow imager and the AIRS satellite experiment, *J. Geophys. Res. Atmos.*, *118*, 3178–3191, doi:10.1002/jgrd.50341.

Yue, J., B. Thurairajah, L. Hoffmann, M. J. Alexander, A. Chandran, M. Taylor, J. M. Russell III, C. Randall, and S. M. Bailey (2014a), Concentric gravity waves in polar mesosphere clouds from the Cloud Imaging and Particle Size (CIPS) experiment, *J. Geophys. Res. Atmos.*, *119*, 5115–5127, doi:10.1002/2013JD021385.

Yue, J., S. D. Miller, L. Hoffmann, and W. C. Straka (2014b), Stratospheric and mesospheric concentric gravity waves over Tropical Cyclone Mahasen: Joint AIRS and VIIRS satellite observations, *J. Atmos. Sol. Terr. Phys.*, *119*, 83–90.